

Article

Numerical and Metallurgical Analysis of Laser Welded, Sealed Lap Joints of S355J2 and 316L Steels under Different Configurations

Hubert Danielewski ^{1,*}, Andrzej Skrzypczyk ¹, Marek Hebda ², Szymon Tofil ¹, Grzegorz Witkowski ¹, Piotr Długosz ³ and Rastislav Nigrovič ⁴

¹ Faculty of Mechatronics and Mechanical Engineering, Kielce University of Technology, Tysiąclecia Państwa Polskiego 7, 25-314 Kielce, Poland; tmaask@tu.kielce.pl (A.S.); tofil@tu.kielce.pl (S.T.); gwitkowski@tu.kielce.pl (G.W.)

² Faculty of Materials Engineering and Physics, Cracow University of Technology, Warszawska 24, 31-155 Cracow, Poland; mhebda@pk.edu.pl

³ Lukaszewicz Network-Cracow Institute of Technology, Zakopiańska 73, 30-418 Cracow, Poland; piotr.dlugosz@kit.lukasiewicz.gov.pl

⁴ Faculty of Mechanical Engineering, Žilinská Univerzita v Žiline Univerzita 1, 010 26 Žilina, Slovakia; rastislav.nigrovic@snop.eu

* Correspondence: hdanielewski@tu.kielce.pl

Received: 18 November 2020; Accepted: 16 December 2020; Published: 20 December 2020



Abstract: This paper presents the results of laser welding of dissimilar joints, where low-carbon and stainless steels were welded in the lap joint configuration. Performed welding of austenitic and ferritic-pearlitic steels included a sealed joint, where only partial penetration of lower material was obtained. The authors presented a comparative study of the joints under different configurations. The welding parameters for the assumed penetration were estimated via a numerical simulation. Moreover, a stress-strain analysis was performed based on the established model. Numerical analysis showed significant differences in joint properties, therefore, further study was conducted. Investigation of the fusion mechanism in the obtained joints was carried out using electron dispersive spectroscopy (EDS) and metallurgical analysis. The study of the lap joint under different configurations showed considerable dissimilarities in stress-strain distribution and relevant differences in the fusion zone structure. The results showed advantages of using stainless steel as the upper material of a microstructure, and uniform chemical element distribution and stress analysis is considered.

Keywords: laser beam welding; sealed lap joints of dissimilar materials; austenitic and ferritic-pearlitic steels; numerical simulation; microstructure analysis

1. Introduction

A number of analytical, numerical, and empirical studies have shown the potential of laser beam welding (LBW). First commercially applied in 1970 [1–3], LBW has become one of the most widely studied techniques of joining metallic parts. A focused laser beam causes rapid vaporization and ionization of the metal. The keyhole effect allows lap welding [4,5]. The weld bead geometry and the joint properties are related to the process parameters and the properties of the welded materials [6,7]. Some process parameters depend on the laser type used (wavelength, transverse mode, pulse/continuous-wave operating mode), the laser machine system (spot size, single or multi-spot optics, focal length), and the programmed parameters (emission frequency, output power, welding speed, focal point position). The material properties, such as thermal conductivity, specific heat capacity, latent heat, and thermal diffusivity, affect the welding dynamics and outcome [8]. The laser beam

penetration is related to the surface reflectivity and the ionization effect of the metal vapor, therefore, the intensity of plasma generation varies for different materials [9]. The beam penetration through two materials is a complex phenomenon, moreover, in dissimilar lap joints, the results of the welding process depend on the welded material configuration.

Numerous studies of laser welding technology, including lap welding, are being carried out. Many of those studies focus on joining special application materials such as titanium, aluminum and nickel-based alloys, zinc-coated steels, or a combination of these materials [10,11]. However, as the researchers focus on one configuration type, there is a lack of publications showing how joint properties change under different configurations. Therefore, the authors presented a comparative study of sealed lap joints with partial penetration, where low-carbon and stainless steels are welded alternately using a laser beam [12]. The joints are intended for use in pipeline components and large crude oil storage tanks, where high joint quality and strength are critical characteristics [13,14].

Nowadays, the development of computing power makes it possible to perform advanced calculations of welding processes, based on the finite element method (FEM) and computer-aided design (CAD) geometry, divided into finite elements (FEs). By solving the heat transfer problem, using differential equations, many physical phenomena, including phase transformation and different heat transfer mechanisms, can be taken into account [15–17]. Nevertheless, in numerical simulations, some parameters cannot be used in the model directly as input data, and some simplifications are necessary [18]. Simple numerical models of laser welding provide a thermal solution where the fusion zone (FZ) and the heat-affected zone (HAZ) dimensions can be calculated. Nevertheless, a more advanced thermo-mechanical solution, a stress–strain analysis, can be carried out. The simulation of a lap joint is complex, and the complexity of the process increases when materials with different thermophysical material properties are to be joined. Realistic results can be obtained by developing an accurate heat source (HS) model and adequate boundary conditions [19,20].

The welding of dissimilar materials is problematic, especially when a sealed lap joint is considered. Many publications report the study of joint properties based on process parameters, while neglecting other aspects [21]. In this paper, the authors proposed a new approach to the problem, by analyzing the joint depending on the configuration of welded materials. On the basis of a numerical simulation, welding parameters were estimated, and stress–strain analysis was performed. The structure of the welds was studied using metallographic and electron dispersive spectroscopy (EDS) analyses. The research showed advantages and disadvantages of austenitic and ferritic-pearlitic steels welded under different configurations in a sealed lap joint.

2. Material and Experimental Design

2.1. Materials

The materials used in the experiment were 4 mm thick steel sheets in grades S355J2 (according to EN 10025-2 [22]) and 316L (according to ASTM A240 [23]), with dimensions of 50 mm × 20 mm. The S355J2 steel is a commonly used, unalloyed, low-carbon construction steel with a ferritic-pearlitic structure. The other material is austenitic stainless steel 316L, with a high content of chromium and nickel. Both steels are characterized as materials of good weld ability, however, the differences in the chemical composition (specified in Table 1) affect the welding process and the properties of the joints.

Table 1. Chemical composition of materials used.

Material	Elements (wt %)										
	C	Mn	Si	P	S	Cr	Ni	Al	Fe	Cu	CEV
S355J2	0.17	1.6	0.02	0.017	0.011	0.02	-	0.05	98.1	0.06	0.45%
316L	0.018	1.57	0.48	0.04	0.002	16.7	11.2	-	balance	-	-

The materials used have different thermophysical properties that are not constant and change with temperature (Figures 1 and 2). This phenomenon affects the laser beam absorption, which increases with material temperature during welding and plays a significant role in the process dynamics. Figures 1 and 2 show the material database with the modified specific heat used to model the latent heat effect, calculated using JMatPro (Sentsoftware, Guildford, Surrey, UK) included in the Simufact Welding 8 software library (MSC Software Company, Hamburg Germany).

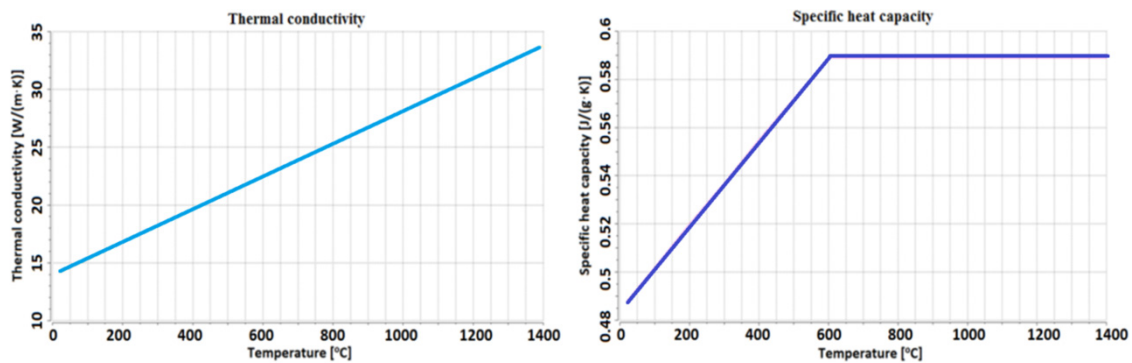


Figure 1. The temperature-dependent thermo-physical properties of 316L steel.

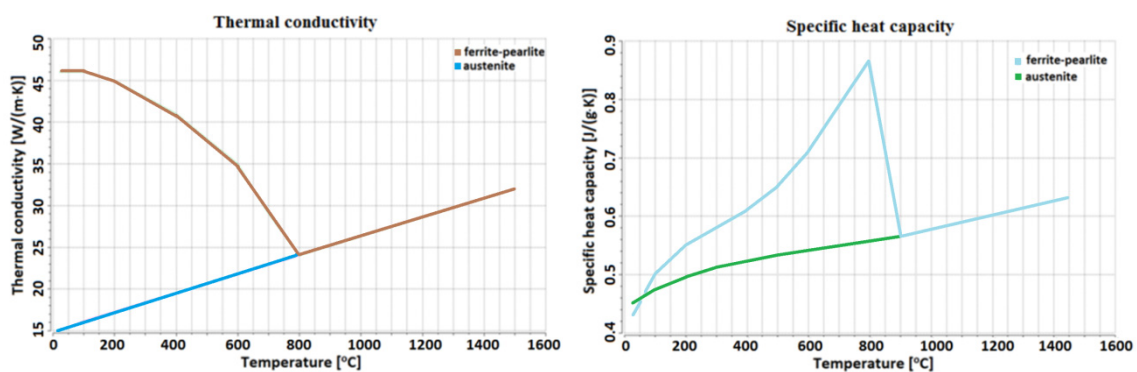


Figure 2. The temperature-dependent thermo-physical properties of S355J2 steel.

The thermophysical properties for the abovementioned materials have a dissimilar range. For austenitic steel, the thermal conductivity uniformly increases in the range of 14 to 34 W/(m·K). Moreover, the specific heat capacity has linear characteristics in the range of 0.49 to 0.59 J/(g·K), and from 600 °C it is linearhorizontal. However, for low-carbon steel, these properties are related to the material phase, and for the austenitic phase, the linear dependence of thermal conductivity in the range from 15 to 33 W/(m·K) can be observed. On the other hand, for the ferrite and pearlite phase, the thermal conductivity decreases from 46 W/(m·K), until it reaches 800 °C, where it overlaps within austenite conductivity. In S355J2 steel, for the austenitic phase, specific heat capacity increases from 0.3 to 0.62 J/(g·K), with a characteristic similar to linear for the ferrite and pearlite phases, and specific heat capacity rapidly increases to 800 °C, reaching the value of 0.86 J/(g·K), and then rapidly decreases; from 900 °C, it overlaps within the austenite value.

2.2. Numerical Simulation Procedure

For a programming simulation of the welding process, particularly LBW, calibration of the HS model is required and, therefore, at the preliminary stage, by comparing the results of trial welding with the simulation, an accurate model was obtained [24]. Software commonly used for welding simulations are based on solving heat-mass flow phenomena (ANSYS with the Fluent module (Ansys Inc., Southpointe, Canonsburg, PA, USA), software with an additional welding module (Abaqus), and software dedicated to welding applications, such as SYSWELD and Simufact Welding [25,26].

From the aforementioned software, Simufact Welding was used for estimating welding parameters, and performing stress and strain analysis. The selected program, based on Marc solver (MSC Software Company, Hamburg Germany), is software dedicated to welding applications, and provides sufficient accuracy of results with a relatively quick calculation time. Simulations of conventional arc welding use the double-ellipsoid Goldak model, however, simulations of laser welding are based on volumetric heat sources (conical and cylindrical), with uneven power distribution (Gaussian parameter). Moreover, some methods use a combination of HSs, with a conical (1) source for simulating the keyhole effect, and a disc-shaped source for simulating laser beam absorption by the material surface (Figure 3) [27,28].

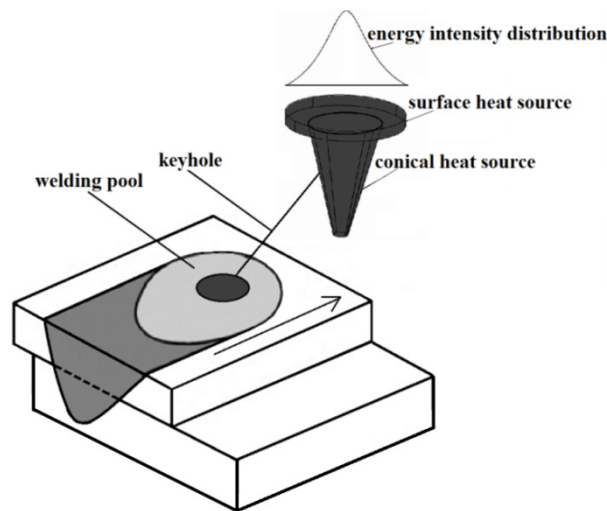


Figure 3. Heatsource model of laser lap joint welding.

Conical volumetric heat source with the Gaussian distribution can be described by the following equation:

$$Q(x, y, z) = Q_0 \exp\left(-\frac{x^2 + y^2}{\left(r_i + \frac{r_t - r_i}{z_t - z_i}(z - z_i)\right)^2}\right) \quad (1)$$

where Q_0 —the maximum heat flux density in a volumetric heat source, $r_t - r_i$ —the dimensions of the upper and lower conical radius, $z_t - z_i$ —the depth of the conical heat source, x, y, z —the heat source coordinates.

Solving the governing heat equation based on Fourier's law for three-dimensional heat conduction (2), with a partial differential equation in a nonlinear form, is done with the following equation:

$$\rho c(T) \frac{\partial T}{\partial t} = \frac{\partial}{\partial x} \left(k(T) \frac{\partial T}{\partial x} \right) + \frac{\partial}{\partial y} \left(k(T) \frac{\partial T}{\partial y} \right) + \frac{\partial}{\partial z} \left(k(T) \frac{\partial T}{\partial z} \right) + q_v \quad (2)$$

where $c(T)$ —temperature-dependent specific heat capacity; $k(T)$ —temperature-dependent thermal conductivity; q_v —volumetric internal energy; x, y, z —space coordinates; T —temperature; ρ —density; and t —time.

The conical heat source can be described as follows:

$$q_l(x, y, z) = \frac{9\eta_l P_l e^3}{\pi(e^3 - 1)(z_t - z_i)(r_t^2 + r_t r_i + r_i^2)} \exp\left(-\frac{3[(x - vt)^2 + y^2]}{\left(r_t - (r_t - r_i) \frac{z_t - z}{z_t - z_i}\right)^2}\right) \quad (3)$$

where q_l —heat flux, $z_t - z_i$ — z coordinates (heat source depth), $r_t - r_i$ —upper and lower conical radius, e —natural logarithm, $r_t - (r_t - r_i) \frac{z_t - z}{z_t - z_i}$ —linear decrease in distribution along the conical heat source, P_l —laser power, η_l —laser heat source efficiency.

Thermal conductivity, specific heat, and emissivity in the heat transfer analysis depend on the temperature, however, the used model is based on the assumption that mass density is constant. By an extrapolating or interpolating procedure, the temperature-dependent properties are averaged. Latent heat is related to phase transformation from solid to liquid metal, or vice versa. Phase change modeling is a complex process, however, using simplification, where latent heat is uniformly released in the solid–liquid range, it can be calculated [29,30].

Due to the convection–diffusion effect involved, the Petro–Galerkin model with nodal velocity vectors was used, which can be described as follows:

$$\frac{\partial T}{\partial t} + v \cdot \nabla T = \nabla \cdot (\kappa \nabla T) + Q \quad (4)$$

where v —nodal velocity vector, T —temperature, κ —diffusion tensor, Q —source term.

The surface energy is determined by calculating the thermal energy that affects the boundary conditions, including thermochemical ablation. These phenomena affect the convective heat flux, and the mass and the enthalpy flow are related to molecular diffusion. The surface energy is correlated with the heat transfer to the material by conduction through a heat-mass flow towards the surface as a result of the evaporation of the material.

Specimens with a size of 50 mm × 20 mm were used for the FE model. Three-dimensional solid hexahedral finite elements were used while meshing. The sizes of the elements were determined by adjusting the resolution and accuracy of the temperature distribution in the regions of severe thermal gradients. A mesh convergence study was performed, within FE sizes of 1.0000, 0.7500, 0.5000, 0.2500, 0.1250, and 0.0625 mm. For 0.0625 and 0.1250 mm, no relevant differences in weld geometry and heat distribution were observed, however, there were some differences between 0.1250 and 0.2500 mm. Therefore, the nominal FE size was set as 0.2500 mm, and in an area where a temperature exceeding 400 °C may occur (Figure 4, region 4), an FE refinement was performed, and the FE size was set as 0.1250 mm. Two 4 mm thick sheets (Figure 4, elements 1 and 2) were oriented in a lap configuration and fixed in three-dimensional space by additional elements (Figure 4, element 3). The welding trajectory was set in the center of the refinement area (9.5 mm from the sheet edge).

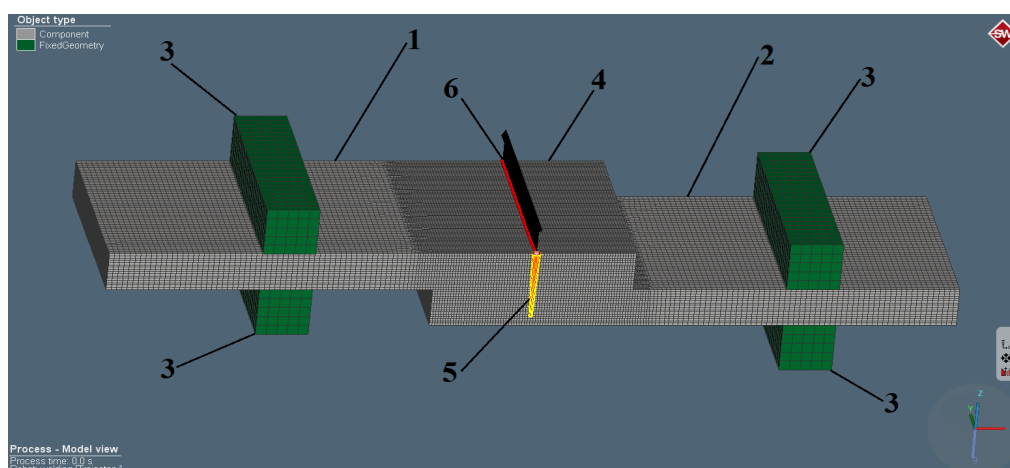


Figure 4. Laser welding finite element (FE) model with defined elements: 1—topsheet 2—bottom sheet, 3—fixed bearings, 4—refined FE area, 5—heat sources, 6—welding trajectory.

The geometries of the heat sources (Figure 3) (3), are related to the used welding optics. In this case, the focal length was equal to 270 mm with a focal point diameter of 0.3 mm. Nevertheless, the HS geometry calibration for obtaining more accurate results was required. Therefore, a trial calibration weld at the speed of 1 m/min and output power equal to 4 kW was performed (to achieve a keyhole effect). A comparison with the simulation results showed a small discrepancy (width of the face of

the weld, with an error less than 15%), and so the heat source geometry was adjusted until the error was less than 1% [31–33]. According to the preliminary calibration performed, a conical heat source with a depth equal to 7 mm, upper radius r_1 equal to 0.4 mm, and lower radius r_2 equal to 0.2 mm, as well as a disc-shaped heat source, with a radius equal to 0.5 mm and depth equal to 0.05 mm, were programmed. The volume heat fraction defined the laser power division between the conical and disc HS and for laser keyhole welding, the value was set as 0.95, which means that 95% of the total power was assigned to the conical HS. Moreover, the Gaussian distribution parameter for the disc HS was defined as 1.0 and for the conical HS as 2.8, and they are related to TEM01* (CO₂ laser, transverse mode). The materials used in the simulation were structural steel of grade S355J2 and 316L austenitic stainless steel. Laser welding with a keyhole effect makes it possible to obtain deep material penetration, however, for a CO₂ laser, the metal surface has high reflectivity and, therefore, HS efficiency for S355J2 was assumed as 0.6, and for 316L as 0.7. The programmed efficiencies are related to laser beam interaction with the materials used, where the reflectivity and the ionization effect have a significant influence on those aspects [34–36].

The simulation of dissimilar, sealed, lap joint laser welding, for two configurations of the top material, was carried out using the Simufact Welding software. Simufact solves a heat transfer problem in solid material, considering the convection–radiation effect, however, no mixing effect of welded material can be taken into account. Figure 5a shows a keyhole in the cross-section during the lap welding, and Figure 5b shows the top hat of the keyhole, during the formation of the face of the weld. The results are presented for the temperature scale in the range of 20 to 3070 °C (from normal condition to the boiling point).

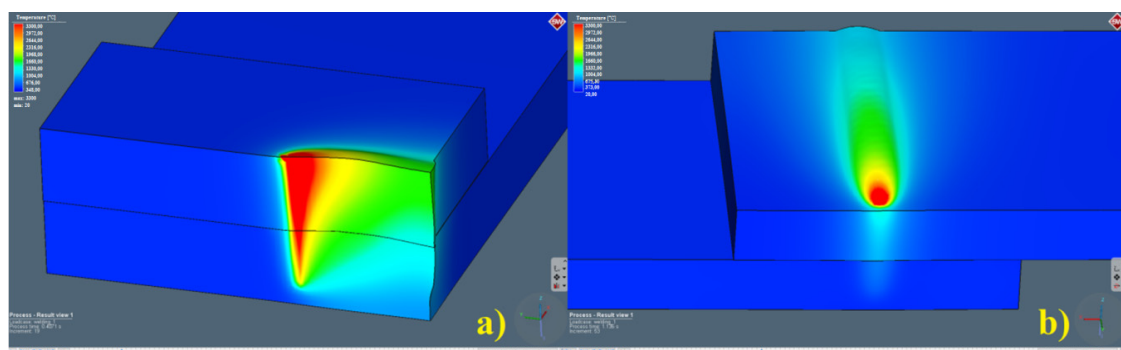


Figure 5. Simulation of laser lap joint welding using the deep penetration mode: (a) view of the keyhole effect in the cross-section, (b) top view of a moving keyhole, and weld formation.

The first joint configuration assumes low-carbon S355J2 steel placed on the top, and the second configuration assumes the opposite: S355J2 steel on the bottom and 316L stainless steel on the top. The research assumed obtaining a sealed lap joint, with partial weld penetration in the bottom sheet [37,38]. Numerical simulations of laser welding were performed at a constant speed of 1 m/min and variable output power in the range of 3 to 6 kW, which increased with each subsequent step by the value of 0.5 kW until the assumed penetration was obtained. The heat source operating time, based on the HS speed and the trajectory length, was equal to 1.2 s, however, the full simulation time, including cooling, was programmed as 30 s. According to the performed simulations, the obtained weld bead geometry and stress–strain distribution (according to the determined measurement points) were studied.

2.3. Experimental Welding Procedure

The first step of the experimental research was the HS validation. For this purpose, a preliminary test according to the procedure described in Section 2.2 was carried out. Based on the aforementioned procedure, calibration of the HS geometry and the efficiency coefficient was carried out. The parameters

estimated in the numerical simulation, welding speed equal to 1 m/min and output power 6 kW, were used to perform trial welds with a TrumpfTruFlow6000 CO₂ CW laser (wavelength 10.6 μm) (Trumpf Group, Ditzingen, German), using welding optics with the focal length of 270 mm and the spot diameter equal to 0.3 mm. This type of laser has worse parameters than fiber or disc lasers, however, further planned research requires the use of single and twin spot optics for an extended weld area, which are available for this type of laser. To shield the welding zone, helium (5.0) was used, with the flow rate equal to 20 l/min conveyed coaxially. The laser beam was focused on the surface of the top plate in a PA (flat) position and the welding trajectory was established based on the boundary conditions of the simulation [39]. Using single pass welding, lap joints in two configurations were obtained: the 1st with the low-carbon steel placed on the top (and the 316L sheet at the bottom), and the 2nd with the 316L steel placed on the top (and the S355J2 sheet at the bottom). Welding procedure qualification was performed according to PN-EN ISO 15609-4: 2009 [40] and the joint quality level was specified according to PN-EN ISO 13919-1 [41]. The results of the simulation and the metallographic analysis of the trial joints were studied.

2.4. Microstructure Analysis

Validation of the simulation results is related to a weld bead build analysis, therefore, measurements of characteristic geometries were carried out. Specimens for further analysis were prepared by cutting them in half (according to the cross-section of the weld), polishing, and etching with Adler reagent. A metallographic analysis of weld structures according to PN-EN ISO 17639 [42], using a Hirox KH-8700 (Hirox Co Ltd., Tokyo, Japan) confocal digital microscope and a scanning electron microscope JSM-7100F (JEOL Ltd., Tokyo, Japan), was carried out. By visual tests and weld bead build evaluation, welding defect detection and inclusion analysis was performed. Investigation of the weld uniformity by element distribution analysis, using a JEOL scanning electron microscope with an electron dispersive X-ray spectroscopy analyzer, was carried out [43].

3. Results

3.1. Global Observation

Due to the significant mismatch of thermal conductivities, specific heat capacity, and surface absorptivities in the welded materials, the FZ and HAZ are different. Moreover, a numerical simulation analysis showed further differences. The research aimed to obtain sealed lap joints, with a bottom sheet welded approximately to 3/4ths of its thickness. A macroscopic analysis showed only partial material mixing in the bottomsheet (Figure 6). The decision of which configuration to choose for better properties is complex and requires an extended thermal stress–strain numerical analysis, as well as micro- and macro-structure examinations. The preliminary visual tests (VTs) showed a good weld build, lack of defects, a convex face of the weld, and assumed partial penetration of the bottom plate was obtained, therefore, according to the requirement of the PN-EN ISO 13919-1 standard, a B quality level was obtained [44,45].

In the obtained welds beads, some separate lap joint characteristic regions were indicated, where: S1—root of the weld, S2—intersheet area, S3—uniform mixing of top plate weld area, S4—HAZ region (Figure 6). Potentially non-uniform mixing of fused materials was detected, which can affect the joint strength and corrosion resistance and can lead to micro-cracking. Therefore, a microstructure analysis, extended to include a numerical stress–strain study for lap welds evaluations, was carried out [46,47].

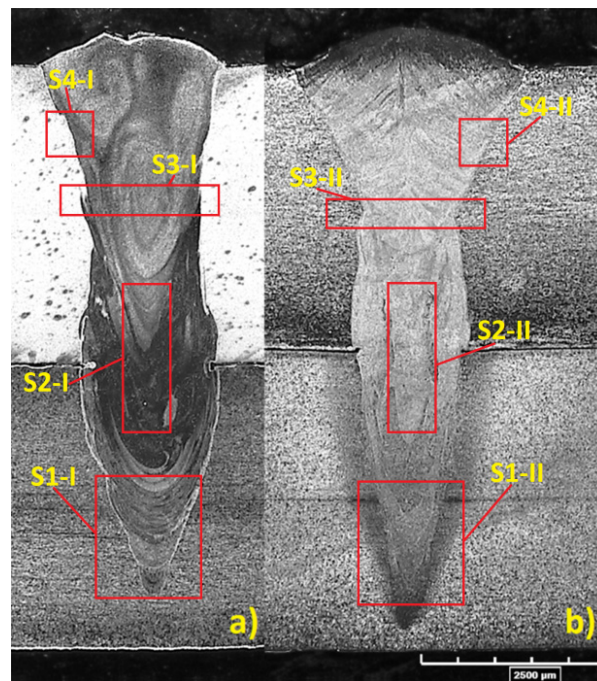


Figure 6. The build of welds with the region defined for further investigation, (a) 1st joint configuration (S355J2 steel on the top), (b) 2nd joint configuration (316L steel on the top).

3.2. Numerical Simulation

The weld bead geometry based on the solid–liquid range was analyzed. On the basis of the programmed HS parameters and established boundary conditions, a numerical simulation of laser lap welding was performed at a constant speed and varying output power. The total thickness of the materials positioned in the lap configuration was equal to 8 mm. As sealed joints were to be obtained, the partial penetration of the weld was up to 7 mm at an output power equal to 6 kW. The differences in the welded materials, especially the absorption coefficient, the thermal conductivity, and the vaporization–ionization effect, made it necessary to change the HS efficiency for each simulation configuration. Therefore, the aforementioned HS efficiency for the low-carbon steel was adopted as 0.6 and for the stainless steel as 0.7 [48,49].

For the 1st configuration, a weld depth equal to 7.1 mm, a weld face width equal to 2.87 mm, and a width of the overlap region equal to 1.92 mm were calculated, with experimental values equal to 7.16 mm, 2.51 mm, and 1.83 mm, respectively (Figure 7). The calculation results for configuration 2 showed similar values, where the depth was equal to 7.15 mm, the weld face width to 3.1 mm, and the width of the overlap region to 1.7 mm. The experimental values were equal to 7.3 mm, 3.15 mm, and 1.59 mm, respectively (Figure 8). Some differences in the weld build were observed. The weld obtained in the 2nd configuration had a typical U-groove weld build, with a wider face of the weld, however, the weld waist was narrower. The 1st configuration showed a narrower face of the weld and a wider weld waist.

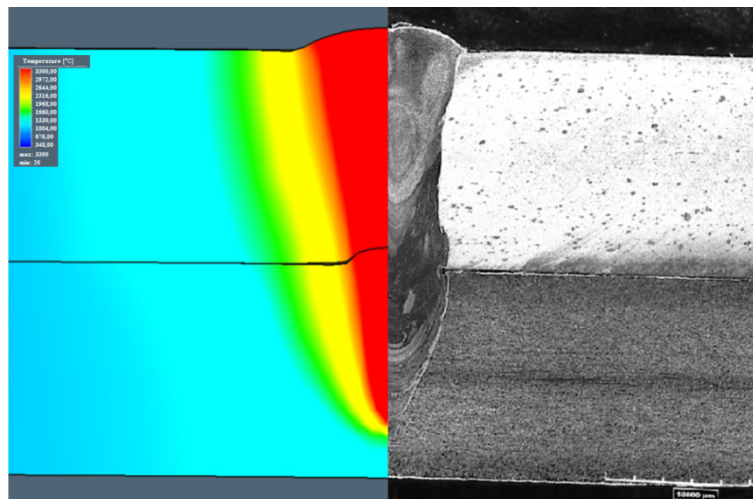


Figure 7. Comparison of the simulation and the trial joint weld build—1st configuration (S355J2 steel on the top).

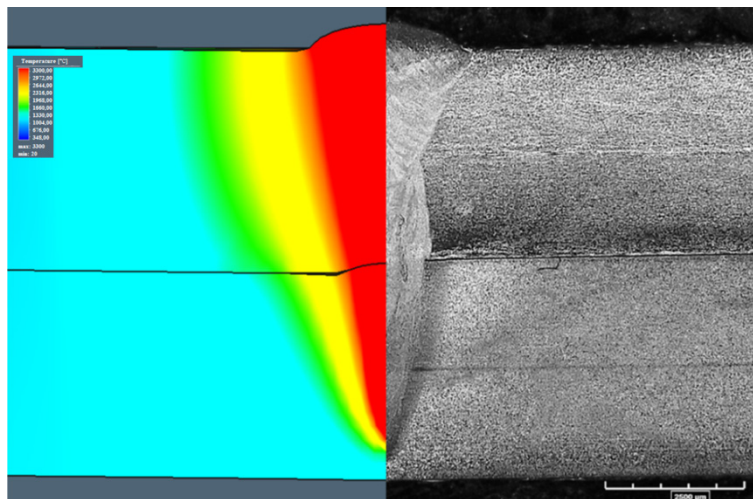


Figure 8. Comparison of the simulation and the trial joint weld build—2nd configuration (316L steel on the top).

Figures 7 and 8 compare the simulation and experimental results. The predicted weld bead geometries were compared to the measurements obtained from the trial joints [50]. The results showed good agreement between the predicted and measured characteristic dimensions of weld geometries.

The studied weld bead build showed some differences but no welding defects or incorrect weld structures were observed. Therefore, in order to decide which configuration gives better results, a further study, starting from a stress–strain distribution analysis, was carried out.

Considering the stress and strain analysis, it is relevant to study the variability of those phenomena in time. Therefore, measurement points, located across determined lines (characteristic joints areas), as shown in Figure 9, were used to perform the analysis, referred to the welding and cooling stages [51–53].

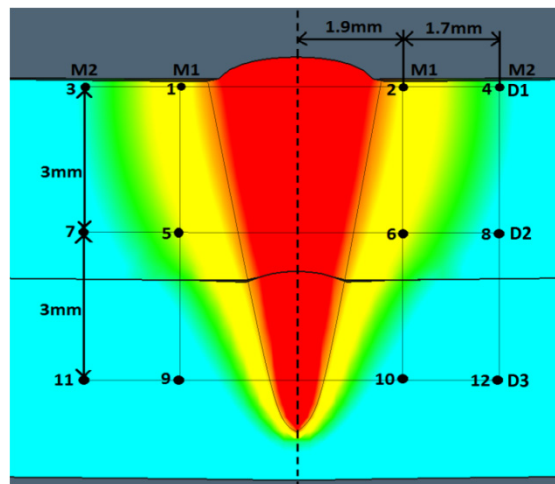


Figure 9. Defined points and lines for stress–strain numerical analysis, selected in critical joint areas.

The measurement points (1–12) were defined along the M1 and M2 measurement lines—parallel to the weld axis, where M1 is the inside line (near fusion line) and M2 is the outside line (near the HAZ line), and D1, D2, and D3 lines are perpendicular to the weld axis, where D1 is the top line, D2 is the central line, and D3 is the bottom line of weld profile. Based on the defined measurement points and lines, a stress–strain analysis for the 1st and 2nd configurations was carried out (Figures 10–14).

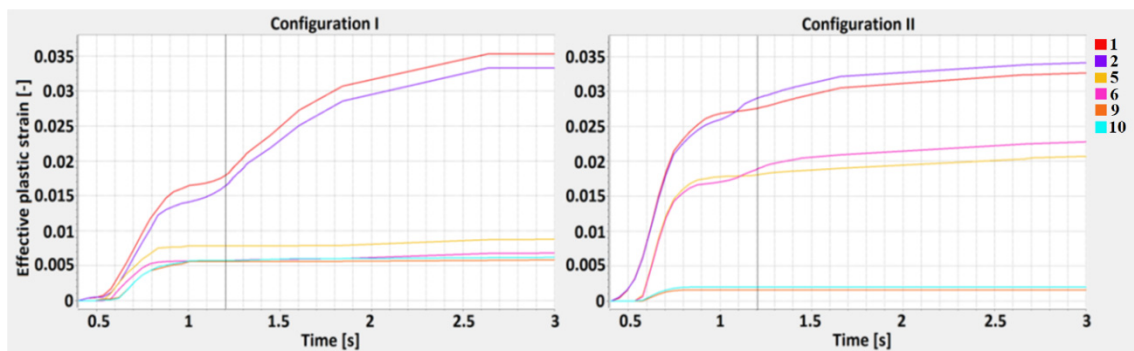


Figure 10. The effective plastic strain curve for the 1st (S355)2 steel on the top) and 2nd (316L steel on the top) configurations along the M1 line.

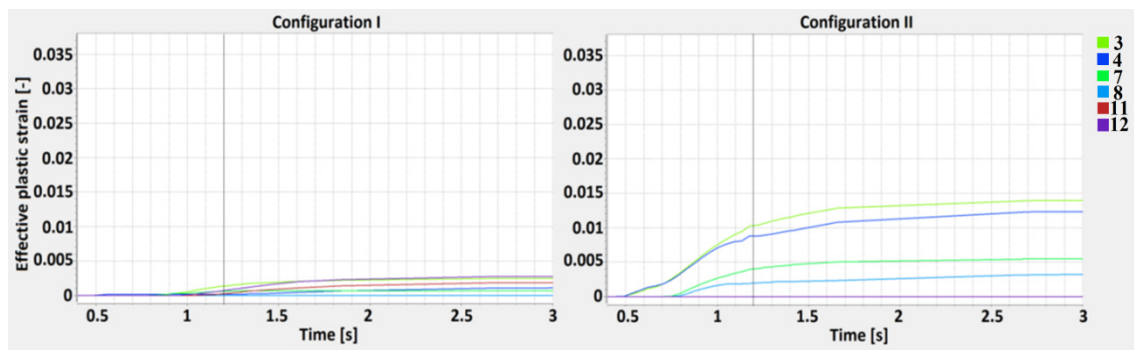


Figure 11. The effective plastic strain curve for the 1st (S355)2 steel on the top) and 2nd (316L steel on the top) configurations along the M2 line.

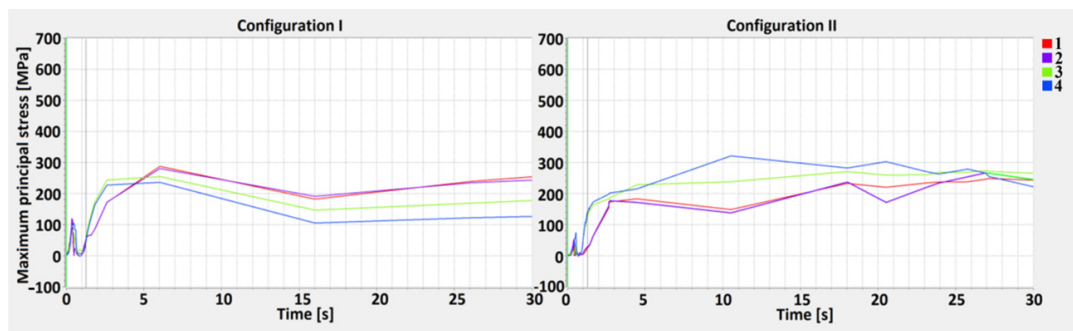


Figure 12. The maximum principal stress curve for the 1st (S355)2 steel on the top) and 2nd (316L steel on the top) configuration along the D1 line—top.

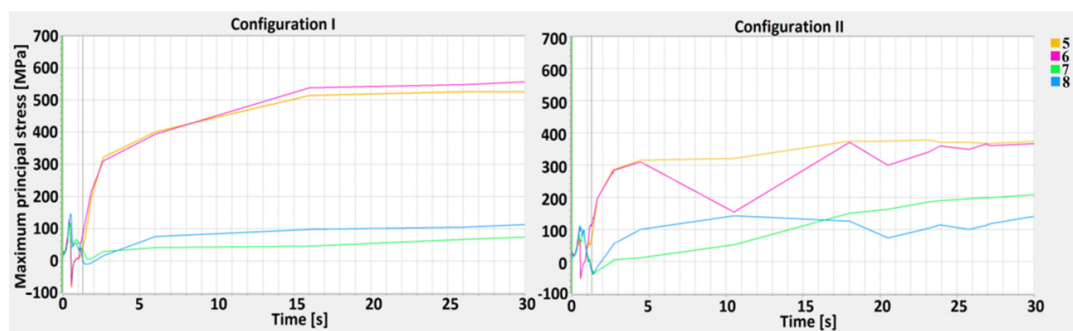


Figure 13. The maximum principal stress curve for the 1st (S355)2 steel on the top) and 2nd (316L steel on the top) configuration along the D2 line—central.

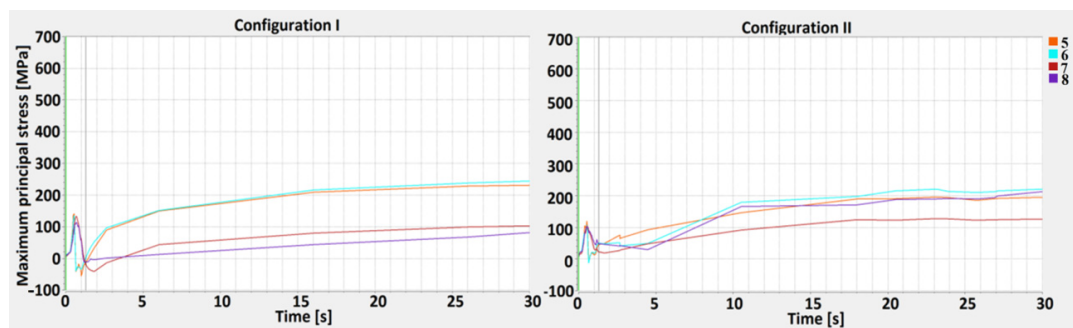


Figure 14. The maximum principal stress curve for the 1st (S355)2 steel on the top) and 2nd (316L steel on the top) configuration along the D3 line—bottom.

Effective plastic strain is a monotonically increasing scalar value which is calculated incrementally, as a function of the plastic component of the rate of the deformation tensor. The effective plastic strain increases whenever the material is actively yielding [54]. An analysis of the effective plastic strain results is shown below, according to the defined M-lines. Welding time alone (1.2 s) during the performed simulation is shown by the perpendicular line.

The tensorial strain values are not monotonically increasing as they reflect the current, the total (elastic+plastic) state of deformation, primarily in the HAZ and across the fusion line where, due to the constituent thermal expansion mismatch, the phase transformation is the most intense. The value of effective plastic strain is the integral of stepwise increments of plastic deformation continuing for a period of time; therefore, the analyzed values are shown according to the welding time. The results show the highest effective plastic strain value across the M1 line and are similar for both joint configurations, however, in the 2nd case, the curve is sharper. The values obtained across the M2 line show greater differences and, in the 2nd configuration, they were almost 4.7 times greater than in

the 1st configuration. While the values for the M1 line obtained at the surface are similar (points 1 and 2), in the central zone of the 1st configuration, they are equal to the bottom zone values (points 5 and 6). For the 2nd configuration, three separate regions of effective plastic strain can be identified. The computation times of the welding process (without cooling) were equal to 1.2 s, therefore, for these specific points, some changes in the plots can be observed [55–57].

A maximum principal stress (MPS) analysis, concerning values changing in time, was performed as well (Figures 12–14). The points selected for the MPS analysis were related to the weld depth (D-lines). By performing a distribution analysis of the maximum principal stress, the areas of stress concentrations can be identified. These particular areas show where crack propagation could start when critical material parameters are reached. An analysis of the results can shown whether in particular joints configurations, the MPS did not exceed the critical values, disqualifying one of the lap joints [58,59].

Analysis of MPS showed higher stress concentrations across the D2 line, particularly in points 5 and 6 (in the middle of the HAZ). The greatest calculated values, equal to 540 MPa, occurred in the 1st configuration, where low-carbon steel is located on the top. In the 2nd configuration, the highest stress occurred across the D2 line as well, however, it did not exceed 400 MPa. At the surface (D1 line), the maximum principal stress exceeded 300 MPa only in point 4. Across the D3 line, the maximum principal stress is similar in both configurations, with slight differences in austenitic steel (in 1st configuration). An increase in the maximum principal stress in D1 and D2 occurred after the welding, and MPS values were related to the movement of the HS, and increased rapidly during the cooling stage, after the heat source was turned off [60–63]. One must keep in mind that the measurement points were located on the sectional plane in the middle of the welding trajectory.

3.3. Metallographic Analysis

Important differences between stress–strain distribution showed significant dissimilarity in joints properties, however, considering only simulation, it is hard to define which configuration provides better results, and further analysis is required. Therefore, the microstructure of characteristic weld areas, chosen alloyed elements distribution (Figure 21), and the precipitates in the fusion zone were studied and the results are shown below.

Figure 15 shows the microstructure of the base material (BM). The structures shown are typical for the used materials, with a ferritic-pearlitic microstructure of low-carbon S355J2 steel (Figure 15a) and an austenitic structure of stainless 316L steel (Figure 15b). The HAZ areas (Figure 16) in both materials are different. In 316L steel, the HAZ is narrow, with grain refining along the fusion line, and an increase in the volume fraction of ferrite δ . The HAZ identified in S355J2 steel is much wider and is made up of three separate regions: overheated zone (OZ), normalization zone (NZ), and partial recrystallization zone (RZ) [64,65]. The HAZ was investigated according to the S3 region (Figure 6).

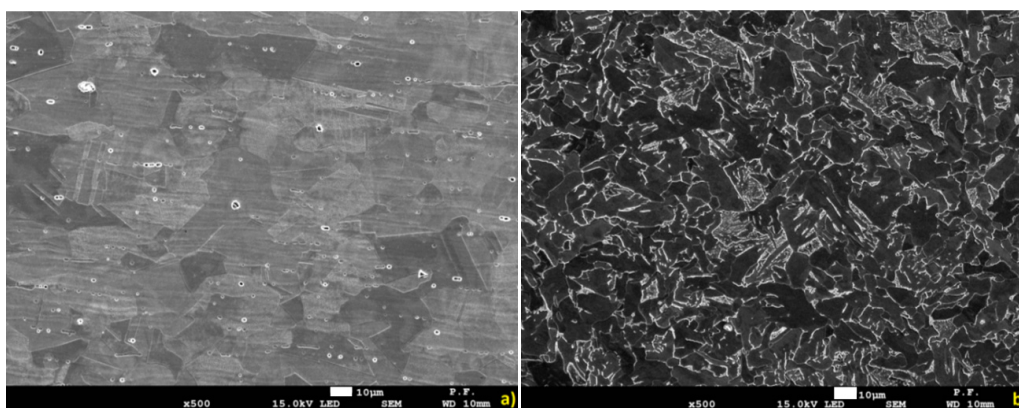


Figure 15. The microstructure of welded base materials: (a) 316L steel, (b) S355J2 steel.

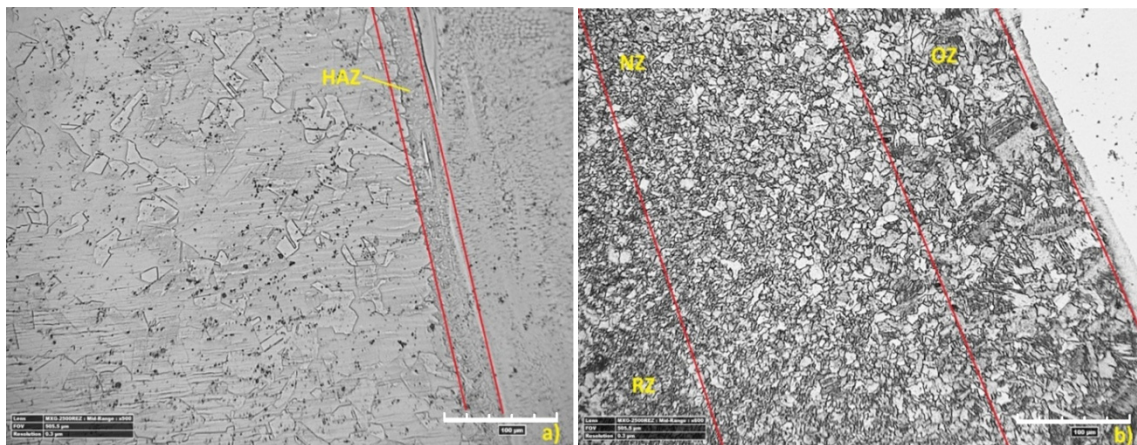


Figure 16. The microstructure of the heat-affected zone (HAZ): (a) 316L steel, (b) S355J2 steel.

The weld composition is related to the mixture of the low-carbon and stainless steel alloying components, and the weld structure is a result of the solidification process of this newly formed material (Figure 17).

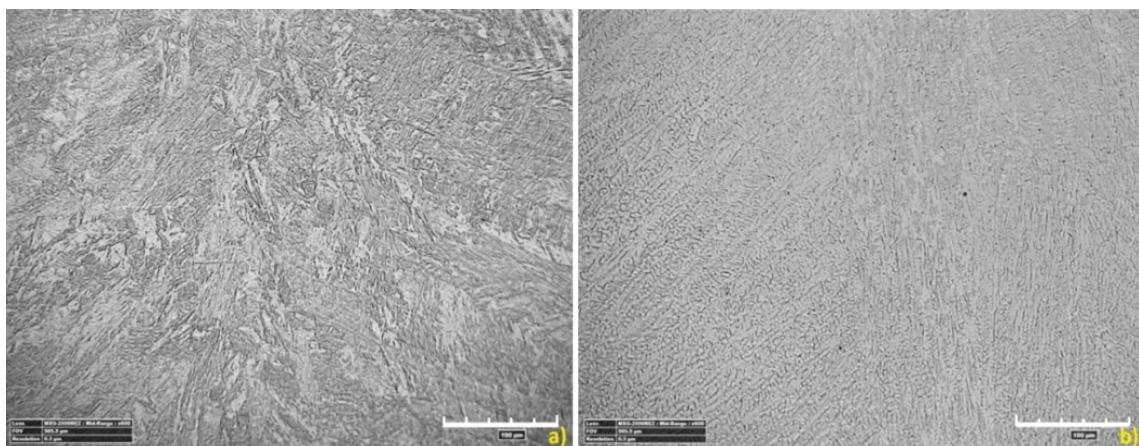


Figure 17. The weld structure approximately in the middle of the upper plate: (a) 1st configuration (S355J2 steel on top), (b) 2nd configuration (316L steel on top).

The obtained structure has a dendritic build, however, in the case where low-carbon steel is the topsheet, the structure is composed of coarse-grained dendrites and acicular ferrite content. Meanwhile, for the configuration where stainless steel is the topsheet, the observed structure has a typical pillar dendritic build. In the 1st case, an austenitic-ferritic structure can be observed, however, in the 2nd case, there is only an austenitic structure. Moreover, fusion zones in the bottom sheet showed regions with non-uniform structures (Figure 18), according to region S1 (Figure 6) [66,67].

The SEM analysis showed differences in the weld structures, where separate areas inside the FZ were identified (Figure 19A,B). In area A, a pillar-dendritic structure was observed, while in area B, a dendritic cellular structure dominated.

In the root of the weld (region S1), where the weld penetration was achieved, some differences were observed. The bottom weld area in austenitic steel had a structure similar to that of the BM (Figure 20a), while in ferritic-pearlitic steel, the structure was similar to that of the HAZ (Figure 20b).

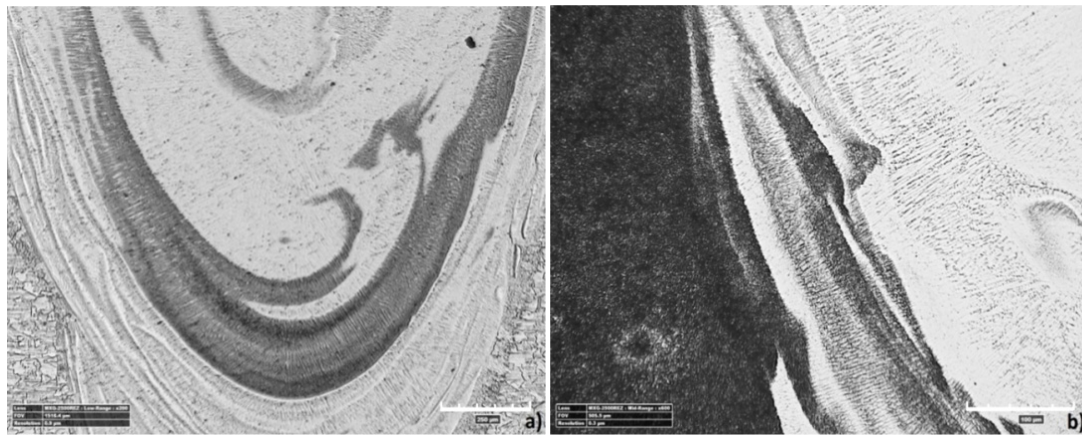


Figure 18. Dissimilarity in the weld structure, down plate: (a) 1st configuration (S355J2 steel on top), (b) 2nd configuration (316L steel on top).

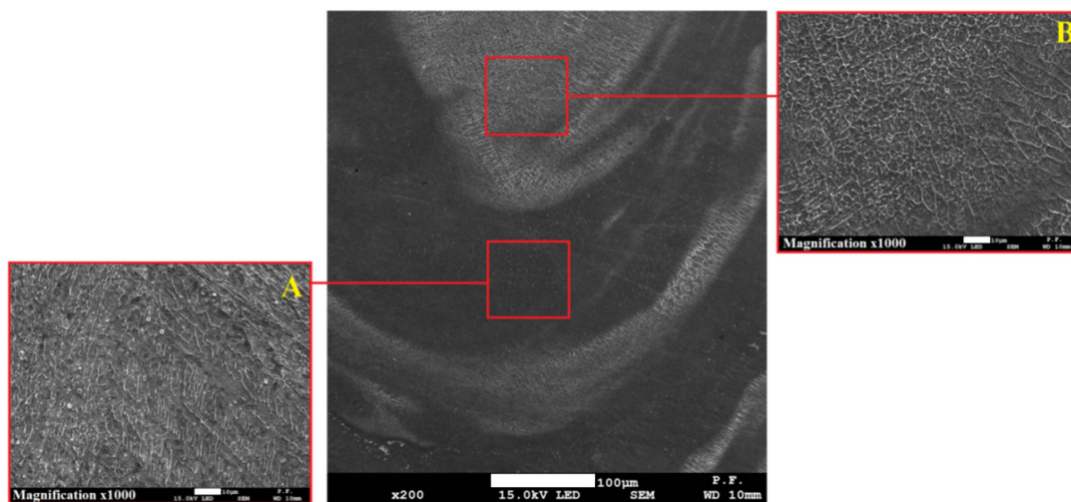


Figure 19. The weld structure approximately in the middle of the down plate, 2nd configuration (316L on top), with identified differences in structure (central picture) and the enlarged areas: (A)—pillar dendritic structure, (B)—cellular dendritic structure.

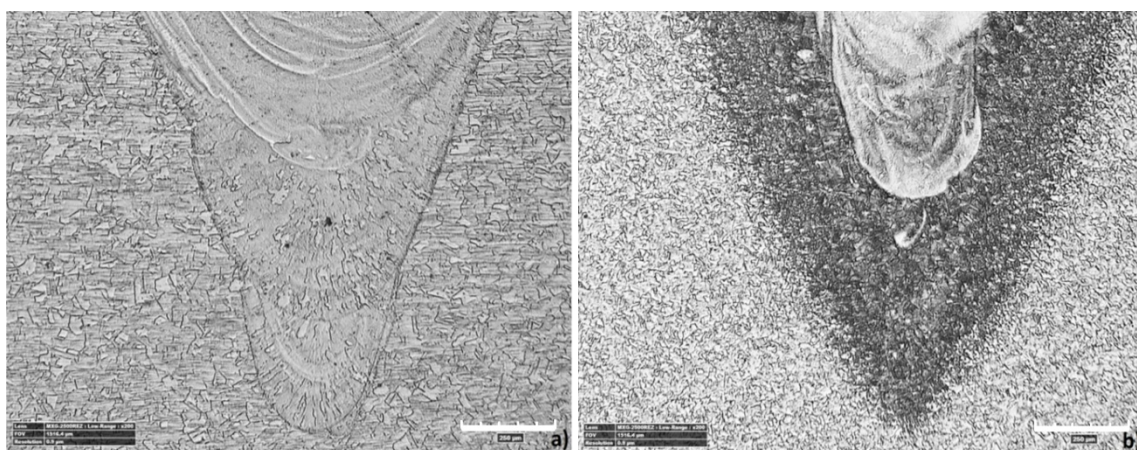


Figure 20. The fusion line of the weld in the down plate: (a) 1st configuration (S355J2 steel on top), (b) 2nd configuration (316L steel on top).

The non-uniform fusion zone structure was confirmed through the EDS analysis. Therefore, according to the defined regions (presented in Figure 6), important differences in chemical composition were studied (Table 1) based on iron, nickel, and chromium distributions in the weld cross-section (Figure 21).

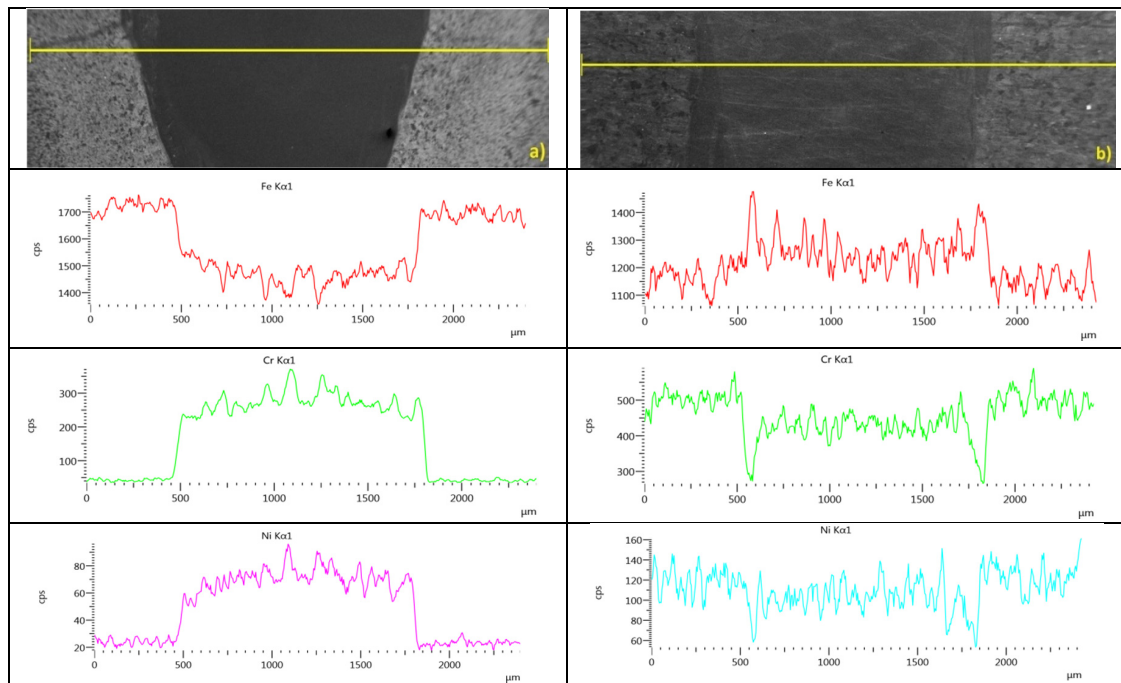


Figure 21. Iron, chromium, and nickel distribution according to S3 region: (a) 1st configuration, (b) 2nd configuration.

The uniform distribution in the topsheet FZ proves the high mixture factor in this region, but the distribution in the bottomsheet FZ is more problematic (Figure 22).

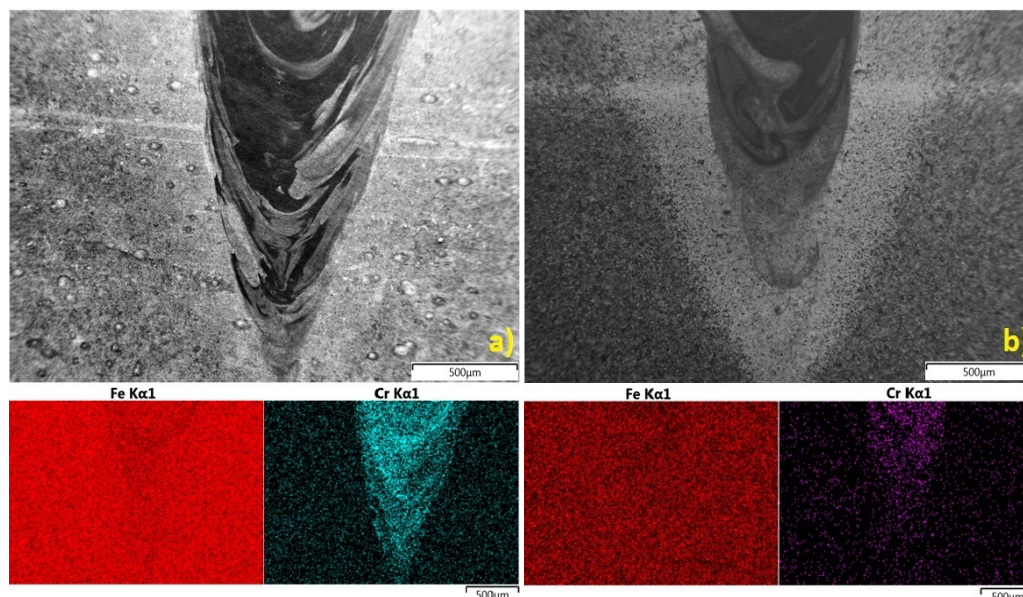


Figure 22. Bottom fusion zone iron and chromium map distribution (region S1): (a) 1st configuration (S355J2 steel on top), (b) 2nd configuration (316L steel on top).

The linear distribution of Fe, Cr, and Ni in the upper plate (region S3) showed greater differences for the 1st configuration (low-carbon steel as the topsheet), while in the 2nd configuration, the distribution was more uniform, however, an analysis showed larger differences in the fusion line region. Moreover, according to the iron and chromium distributions, the joints made in the 1st configuration showed low iron content and a large amount of chromium, while in the 2nd configuration, the iron distribution was almost uniform, with slightly increased chromium content.

4. Discussion

The welded materials have important differences in thermo-physical properties related to their chemical composition (Table 1). Both materials are characterized by good weldability, but due to the differences discussed above, joining them by welding is problematic, especially when we consider a lap joint with partial penetration in the bottom plate, as described in this paper.

Global observation showed differences in the weld builds for both assumed joint configurations. The macroscopic analysis showed a potentially non-uniform structure in the fusion zones. Therefore, in order to investigate the quality level of the joints and to choose which configuration gives better results, numerical analysis and then metallographic studies were carried out.

Based on the developed numerical model, calibrated in the preliminary research, the welding parameters for the sealed lap joint were estimated. According to the established boundary conditions and the programmed simulation parameters, welding speed equal to 1 m/min with 6 kW of output power results in the assumed partial penetration. The performed simulations provided results where the differences in the width of the face of the weld were less than 14.5% compared to the trial joint for the 1st configuration and 1.62% for the 2nd configuration. The difference in the weld depth, calculated and obtained via experimental welding for the 1st configuration, was equal to 0.85% and for the 2nd configuration, to 2.1%. The width of the overlap region resulted in a 4.9% mismatch, comparing the simulation and the trial joint results for the 1st configuration, and 6.9% for the 2nd configuration. The numerical model obtained gave accurate results of the estimated weld bead geometry, however, the mismatch in the weld width for the 1st configuration, where low-carbon S355J2 steel was the topsheet, resulted in a 14.5% difference. The numerical model did not include the Marangoni effect and the surface tension, which has a great impact on the face of weld geometry. However, based on the small differences in other (Figures 7 and 8) weld geometries, the established model gave realistic results and was used for joint stress–strain analysis [68–70].

In order to define the properties of the obtained joints based on the simulation results, the distribution of the effective plastic strain and the maximum principal stress was studied according to the determined lines (Figure 9). The M lines define points distributed parallel to the weld, near the fusion and heat-affected zones lines, and D lines are related to the weld penetration depth and are distributed perpendicular to the weld axis. According to the M1 and M2 lines, the effective plastic strain analysis showed a maximum value equal to 0.035 and was similar for both joint configurations, however, in the 2nd case, the values increased more rapidly. For the 1st case, the increase was slower, however, after the end of the welding cycle (1.2 s), it was still rising in the cooling stage, to 2.6 s. For the M2 lines (located 3.6 mm from the weld axis), the effective plastic strains were much smaller and the maximum calculated value (which occurred in the 2nd configuration) did not exceed 0.015, while for the 1st configuration, it was equal to 0.03. The differences in the effective plastic strain can be related to the different values of thermal conductivity (curves from 0 to 1.2 s), which for low-carbon steel resulted in a higher accumulation of thermal energy in the fusion zone and phase transformation (after 1.2 s) in the cooling stage [71].

The maximum principal stress values across the D lines showed that the stress characteristic was divided into two separate cycles. The first was related to heating and cooling during movement of the HS, however, this value did not exceed 150 MPa. The second was related to material cooling, when the heat source was turned off. The maximum principal stress increased on the surface of the topsheet and its value ranged from 60 to 290 MPa for the 1st configuration and 20 to 320 MPa for the 2nd

(the curve characteristics were similar for all measurement points). In the center line (D2), a greater stress value occurred in joint configuration number 1 and was equal to 540 MPa, while for the 2nd configuration, the value did not exceed 400 MPa. For the D3 lines, the values were less than 240 MPa (1st configuration) and equal to 200 MPa (2nd configuration). The maximum principal stress had a greater value in the measurement points located closer to the weld axis, with the greatest difference occurring across the D2 line, where at points 5 and 6 they were more than 5.5 times greater than in points 7 and 8. The calculated maximum principal stress had a greater value in the 1st configuration and was related to the thermal gradient and the phase transformation of low-carbon steel [72,73].

A metallographic analysis confirmed the typical structure of the welded materials in the BM region, austenitic in 316L steel and ferritic-pearlitic in S355J2 steel. Significant differences in the heat-affected zones were observed. In stainless steel, the HAZ was very narrow and no growth of austenite grains was observed, while the elongated grains of the ferrite formed a discontinuous network around the austenite grains. These regions occur in steels with the structure of a native material consisting of austenite with the participation of ferrite δ . At high temperatures near the fusion line, the transformation of $\gamma \rightarrow \delta$ occurs, which begins in the existing ferrite δ grains and progresses in areas with increased chromium concentration. After re-cooling, these areas do not achieve an equilibrium structure and the proportion of ferrite δ is increased. The HAZ of low-carbon steel is considerably wider and is made up of three regions: an overheated zone, a normalization zone, and a partial recrystallization zone. These phenomena are related to phase transformation and structural changes during the solidification and cooling process. The obtained HAZs (including microstructure and geometry) of welded materials are typical for this steel grade welded using the LBW method [74].

In the global observation, some non-uniform microstructure of the fusion zones was detected, therefore, an extended weld microstructure analysis was carried out. The structure observed in the topsheet FZ had a typical uniform dendritic build, however, in the 1st configuration, coarse-grained dendrites containing acicular ferrite were observed, while in the 2nd configuration, a typical pillar-dendritic build occurred. When the keyhole only partially penetrates the bottom workpiece, the influence of the flow field is clearly evident from the corresponding solidified structure. In the case of partial penetration, discrete growth bands occurred in the entire solidified weld bead, suggesting severe fluctuations in the flow field and the growth process [75]. On the contrary, in the topsheet, a full penetration keyhole was performed, where a columnar structure and an equiaxed zone along the centerline, similar to that shown in Figure 17b, can be observed. Discrete growth bands or striations occurred occasionally in this case, but the structural pattern was maintained within these bands. It should be noted that the laser output power in both cases was similar.

The fusion zone structure in the overlap region are similar to those observed in the FZ upper region, however, in the bottom plate, non-uniform structures were identified (Figure 18). There were differences in the fusion structure (Figure 19), where a pillar-dendritic build in region A and a cellular-dendritic structure in region B were observed. In the root of the weld, at the bottom of the fusion zone where weld penetration reaches, the structure was similar to the BM for stainless steel and the HAZ structure for low-carbon steel. In this region, the temperature exceeded the melting point, but only slightly, and according to the direction of heat diffusion in the XYZ axis, the heat flow to the BM was higher [76].

Homogenous weld builds are related to the uniform distribution of chemical elements. The welded materials have important differences in chemical composition, where S355J2 steel has a high content of iron and only trace amounts of chromium and nickel, while stainless steel contains more than 16% chromium, 11% nickel, and a balanced content of iron. Therefore, an analysis of defined regions in the cross-section of the welds was performed based on the linear and map distribution of these elements. The study showed bigger differences between the BM and the FZ in the distribution of Fe, Cr, and Ni in the 1st configuration. A clear boundary between the base material and the fusion zone was observed, however, the distribution curve had an almost vertical characteristic. For the 2nd configuration, the differences were smaller, with peak changes along the fusion line, which is related to chromium diffusion and concentration across the fusion line (phase transformation and increasing

content of ferrite δ). An EDS analysis of the FZ bottom region showed further differences, particularly in chromium and iron distribution [77]. For the 1st configuration, small amounts of iron were detected and considerably greater differences in the detection of chromium were observed (Figure 22a). In the 2nd joint configuration, the iron distribution in the fusion zone and the base material was almost uniform, and some differences in chromium detection were observed (Figure 22b).

5. Conclusions

The study of laser lap joint welding, where low-carbon S355J2 and stainless 316L steel were joined together in two configurations (1st with low-carbon steel on the top, 2nd with stainless steel on the top), showed significant differences in the obtained results. According to the developed numerical model and the established boundary conditions, an accurate match of the simulated and experimental results of weld geometry was obtained. Assuming that the obtained model gave accurate results, a numerical stress–strain analysis was performed. Higher values of effective plastic strain occurred in the 2nd configuration, however, the maximum principal stress values were greater in the 1st configuration. Greater differences in the measurement points occurred for the configuration with low-carbon steel placed on the top. The microstructure analysis showed further differences, most of all in the fusion zone structure, where in the bottom plate, two separate structures were detected. A more uniform structure was observed in the 1st configuration, however, greater differences in Cr, Ni, and Fe distribution between the FZ and the BM were detected in this configuration. No porosity, cracks, or welding defects were identified, therefore, according to the requirement of PN-EN ISO 13919-1, a B quality level was assumed. According to the performed study, and based on the maximum principal stress distribution, differences in the weld structure, and the distribution of the alloying elements, the second configuration showed better properties. Therefore, the second configuration, where stainless steel is placed on the top, was chosen as a dominant joint. The microstructure study showed a non-uniform mixture of welded material in the root of the weld, however, no welding defects or precipitations in the inter-plate region were observed. This study confirms the impact of the welded material configuration on joint properties and shows which configuration ensures the lowest stress and strain concentration and a more uniform weld structure. Therefore, according to:

- calculated maximum principal stress value.
- lower differences in the chemical element distribution in the weld.
- more uniform structure and fusion rate in the weld.

When laser lap welding of S355J2 and 316L steels is considered, the configuration in which stainless steel is placed on top provides better joint properties and is recommended. The presented results showed that when a high-quality steel joint with good strength characteristics is required, such as pipeline components or crude oil storage tanks, the welding position should be related to the stainless steel side.

Further investigation of this joint type is required, therefore, the possibility of using twin spot laser welding optics is planned. The research will also be extended to mechanical tests, including the tensile strength and hardness tests.

Author Contributions: Conceptualization, H.D., A.S., and R.N.; methodology, H.D., A.S., M.H., and P.D.; software, H.D., G.W., and S.T.; validation, H.D., A.S., M.H., P.D., and R.N.; formal analysis, H.D., A.S., R.N., S.T., and P.D.; investigation, H.D. and G.W.; resources, H.D.; writing—original draft preparation, H.D., A.S., M.H., P.D., and R.N.; writing—review and editing, H.D., A.S., M.H., and G.W.; visualization, H.D. and G.W.; revision, A.S. and M.H.; project administration, H.D.; funding acquisition, H.D. All authors have read and agree to the published version of the manuscript.

Funding: This research was funded by NCBiR, grant number LIDER/31/0173/L-8/16/NCBR/2017: Technology of manufacturing sealed weld joints for gas installation by using concentrated energy source.

Conflicts of Interest: The authors declare no conflict of interest.

References

1. Mazumder, J. Laser Welding: State of the Art Review. *JOM* **1982**, *34*, 16–24. [[CrossRef](#)]
2. Mohanty, P.S.; Mazumder, J. Workbench for keyhole laser welding. *Sci. Technol. Weld. Join.* **1997**, *2*, 133–138. [[CrossRef](#)]
3. Matsunawa, A. Problems and solutions in deep penetration laser welding. *Sci. Technol. Weld. Join.* **2001**, *6*, 351–354. [[CrossRef](#)]
4. Yang, R.-T.; Chen, Z.-W. A study on fiber laser lap welding of thin stainless steel. *Int. J. Precis. Eng. Manuf.* **2013**, *14*, 207–214. [[CrossRef](#)]
5. Khan, M.; Romoli, L.; Fiaschi, M.; Sarri, F.; Dini, G. Experimental investigation on laser beam welding of martensitic stainless steels in a constrained overlap joint configuration. *J. Mater. Process. Technol.* **2010**, *210*, 1340–1353. [[CrossRef](#)]
6. Meco, S.; Pardal, G.; Ganguly, S.; Williams, S.W.; McPherson, N. Application of laser in seam welding of dissimilar steel to aluminium joints for thick structural components. *Opt. Lasers Eng.* **2015**, *67*, 22–30. [[CrossRef](#)]
7. Takano, K.; Koizumi, N.; Serizawa, H.; Tsubota, S.; Makino, Y. Development of laser welding technology for fully austenitic stainless steel. *Weld. Int.* **2017**, *31*, 827–836. [[CrossRef](#)]
8. Tan, W.; Shin, Y.C. Laser keyhole welding of stainless steel thin plate stack for applications in fuel cell manufacturing. *Sci. Technol. Weld. Join.* **2015**, *20*, 313–318. [[CrossRef](#)]
9. Kouraytem, N.; Li, X.; Cunningham, R.; Zhao, C.; Parab, N.; Sun, T.; Rollett, A.D.; Spear, A.D.; Tan, W. Effect of Laser-Matter Interaction on Molten Pool Flow and Keyhole Dynamics. *Phys. Rev. Appl.* **2019**, *11*, 064054. [[CrossRef](#)]
10. Lisiecki, A.; Wójciga, P.; Kurc-Lisiecka, A.; Barczyk, M.; Krawczyk, S. Laser welding of panel joints of stainless steel heat exchangers. *Weld. Technol. Rev.* **2019**, *91*, 7–19. [[CrossRef](#)]
11. Szczepaniak, A.; Fan, J.; Kostka, A.; Raabe, D. On the Correlation between Thermal Cycle and Formation of Intermetallic Phases at the Interface of Laser-Welded Aluminum-Steel Overlap Joints. *Adv. Eng. Mater.* **2012**, *14*, 464–472. [[CrossRef](#)]
12. Oussaid, K.; El Ouafi, A.; Chebak, A. Experimental Investigation of Laser Welding Process in Overlap Joint Configuration. *J. Mater. Sci. Chem. Eng.* **2019**, *7*, 16–31. [[CrossRef](#)]
13. Noga, P.; Węglowski, M.; Zimierska-Nowak, P.; Richert, M.; Dworak, J.; Rykała, J. Influence of welding techniques on microstructure and hardness of steel joints used in automotive air conditioners. *Met. Foundry Eng.* **2017**, *43*, 281. [[CrossRef](#)]
14. Guo, W.; Kar, A. Determination of weld pool shape and temperature distribution by solving three-dimensional phase change heat conduction problem. *Sci. Technol. Weld. Join.* **2000**, *5*, 317–323. [[CrossRef](#)]
15. Wang, R.; Lei, Y.; Shi, Y. Numerical simulation of transient temperature field during laser keyhole welding of 304 stainless steel sheet. *Opt. Laser Technol.* **2011**, *43*, 870–873. [[CrossRef](#)]
16. Dal, M.; Fabbro, R. An overview of the state of art in laser welding simulation. *Opt. Laser Technol.* **2016**, *78*, 2–14. [[CrossRef](#)]
17. Shanmugam, N.S.; Buvanashakaran, G.; Sankaranarayanan, K.; Manonmani, K. Some studies on temperature profiles in AISI 304 stainless steel sheet during laser beam welding using FE simulation. *Int. J. Adv. Manuf. Technol.* **2008**, *43*, 78–94. [[CrossRef](#)]
18. Schöler, C.; Haeusler, A.; Karyofylli, V.; Behr, M.; Schulz, W.; Gillner, A.; Niessen, M. Hybrid simulation of laser deep penetration welding. *Mater. Werkst.* **2017**, *48*, 1290–1297. [[CrossRef](#)]
19. Miyashita, Y.; Mutoh, Y.; Akahori, M.; Okumura, H.; Nakagawa, I.; Jin-Quan, X. Laser welding of dissimilar metals aided by unsteady thermal conduction boundary element method analysis. *Weld. Int.* **2005**, *19*, 687–696. [[CrossRef](#)]
20. Evdokimov, A.; Springer, K.; Doynov, N.; Ossenbrink, R.; Michailov, V. Heat source model for laser beam welding of steel-aluminum lap joints. *Int. J. Adv. Manuf. Technol.* **2017**, *93*, 709–716. [[CrossRef](#)]
21. Ozkat, E.C.; Franciosa, P.; Ceglarek, D. Development of decoupled multi-physics simulation for laser lap welding considering part-to-part gap. *J. Laser Appl.* **2017**, *29*, 22423. [[CrossRef](#)]
22. EN 10025-2: Hot rolled products of structural steels. In *Technical Delivery Conditions for Non-Alloy Structural Steels*; PKN: Warsaw, Poland, 2007.

23. ASTM A240/A240M-18: *Standard Specification for Chromium and Chromium-Nickel Stainless Steel Plate, Sheet, and Strip for Pressure Vessels and for General Applications*; ASTM: West Conshohocken, PA, USA, 2018.
24. Chen, C.; Lin, Y.-J.; Ou, H.; Wang, Y. Study of Heat Source Calibration and Modelling for Laser Welding Process. *Int. J. Precis. Eng. Manuf.* **2018**, *19*, 1239–1244. [[CrossRef](#)]
25. Derakhshan, E.D.; Yazdian, N.; Craft, B.; Smith, S.; Kovacevic, R. Numerical simulation and experimental validation of residual stress and welding distortion induced by laser-based welding processes of thin structural steel plates in butt joint configuration. *Opt. Laser Technol.* **2018**, *104*, 170–182. [[CrossRef](#)]
26. De, A.; Maiti, S.K.; Walsh, C.A.; Bhadeshia, H.K.D.H. Finite element simulation of laser spot welding. *Sci. Technol. Weld. Join.* **2003**, *8*, 377–384. [[CrossRef](#)]
27. Phanikumar, G.; Chattopadhyay, K.; Dutta, P. Joining of dissimilar metals: Issues and modelling techniques. *Sci. Technol. Weld. Join.* **2011**, *16*, 313–317. [[CrossRef](#)]
28. Mayboudi, L.; Birk, A.; Zak, G.; Bates, P. A Three-Dimensional Thermal Finite Element Model of Laser Transmission Welding for Lap-Joint. *Int. J. Model. Simul.* **2009**, *29*, 149–155. [[CrossRef](#)]
29. Shanmugam, N.S.; Buvanashakaran, G.; Sankaranarayanan, K.; Kumar, S.R. A Transient Finite Element Simulation of the Temperature Field and Bead Profile of T-Joint Laser Welds. *Int. J. Model. Simul.* **2010**, *30*, 108–122. [[CrossRef](#)]
30. Farrokhi, F.; Endelt, B.; Kristiansen, M. A numerical model for full and partial penetration hybrid laser welding of thick-section steels. *Opt. Laser Technol.* **2019**, *111*, 671–686. [[CrossRef](#)]
31. Mazumder, J.; Steen, W.M. Heat transfer model for cw laser material processing. *J. Appl. Phys.* **1980**, *51*, 941. [[CrossRef](#)]
32. Torkamany, M.J.; Sabbaghzadeh, J.; Hamed, M. Effect of laser welding mode on the microstructure and mechanical performance of dissimilar laser spot welds between low carbon and austenitic stainless steels. *Mater. Des.* **2012**, *34*, 666–672. [[CrossRef](#)]
33. Sudnik, W.; Radaj, D.; Breitschwerdt, S.; Erofeev, W. Numerical simulation of weld pool geometry in laser beam welding. *J. Phys. D Appl. Phys.* **2000**, *33*, 662–671. [[CrossRef](#)]
34. Phaonaim, R.; Yamamoto, M.; Shinozaki, K.; Yamamoto, M.; Kadoi, K. Development of a Heat Source Model for Narrow-gap Hot-wire Laser Welding. *Q. J. Jpn. Weld. Soc.* **2013**, *31*, 82s–85s. [[CrossRef](#)]
35. Carmignani, C.; Mares, R.; Toselli, G. Transient finite element analysis of deep penetration laser welding process in a singlepass butt-welded thick steel plate. *Comput. Methods Appl. Mech. Eng.* **1999**, *179*, 197–214. [[CrossRef](#)]
36. Kano, S.; Oba, A.; Yang, H.-L.; Matsukawa, Y.; Satoh, Y.; Serizawa, H.; Sakasegawa, H.; Tanigawa, H.; Abe, H. Experimental assessment of temperature distribution in heat affected zone (HAZ) in dissimilar joint between 8Cr-2W steel and SUS316L fabricated by 4 kW fiber laser welding. *Mech. Eng. Lett.* **2016**, *2*, 15. [[CrossRef](#)]
37. Shanmugam, N.S.; Buvanashakaran, G.; Sankaranarayanan, K. Experimental investigation and finite element simulation of laser beam welding of AISI 304 stainless steel sheet. *Exp. Tech.* **2009**, *34*, 25–36. [[CrossRef](#)]
38. Danielewski, H.; Skrzypczyk, A. Steel Sheets Laser Lap Joint Welding—Process Analysis. *Materials* **2020**, *13*, 2258. [[CrossRef](#)]
39. Oh, R.; Kim, D.Y.; Ceglarek, D. The Effects of Laser Welding Direction on Joint Quality for Non-Uniform Part-to-Part Gaps. *Materials* **2016**, *6*, 184. [[CrossRef](#)]
40. PN-EN ISO 15609-4: 2009: *Specification and Qualification of Welding Procedures for Metallic Materials-Welding Procedure Specification-Part 4: Laser Beam Welding*; PKN: Warsaw, Poland, 2009.
41. PN-EN ISO 13919-1: 2002: *Welding-Electrons and Laser Beam Welded Joints-Guidance on Quality Levels for Imperfections-Part 1: Steel*; PKN: Warsaw, Poland, 2002.
42. PN-EN ISO 17639:2013: *Destructive Tests on Welds in Metallic Materials-Macroscopic and Microscopic Examination of Welds*; PKN: Warsaw, Poland, 2013.
43. Rong, Y.; Xu, J.; Lei, T.; Wang, W.; Sabbar, A.A.; Huang, Y.; Wang, C.; Chen, Z. Microstructure and alloy element distribution of dissimilar joint 316L and EH36 in laser welding. *Sci. Technol. Weld. Join.* **2018**, *23*, 454–461. [[CrossRef](#)]
44. Kuryntsev, S.V. Microstructure, mechanical and electrical properties of laser-welded overlap joint of CP Ti and AA2024. *Opt. Lasers Eng.* **2019**, *112*, 77–86. [[CrossRef](#)]
45. Tsoukantas, G.; Chryssoulouris, G. Theoretical and experimental analysis of the remote welding process on thin, lap-joined AISI 304 sheets. *Int. J. Adv. Manuf. Technol.* **2008**, *35*, 880–894. [[CrossRef](#)]

46. Kubiak, M.; Piekarska, W.; Stano, S.; Saternus, Z. Numerical Modelling of Thermal And Structural Phenomena In Yb:YAG Laser Butt-Welded Steel Elements. *Arch. Met. Mater.* **2015**, *60*, 821–828. [[CrossRef](#)]
47. Ferro, P.; Bonollo, F.; Tiziani, A. Laser welding of copper–nickel alloys: A numerical and experimental analysis. *Sci. Technol. Weld. Join.* **2005**, *10*, 299–310. [[CrossRef](#)]
48. Huang, B.-S.; Yang, J.; Lu, D.-H.; Bin, W.-J. Study on the microstructure, mechanical properties and corrosion behaviour of S355JR/316L dissimilar welded joint prepared by gas tungsten arc welding multi-pass welding process. *Sci. Technol. Weld. Join.* **2016**, *21*, 381–388. [[CrossRef](#)]
49. Brand, M.; Siegele, D. Numerical Simulation of Distortion and Residual Stresses of Dual Phase Steels Weldments. *Weld. World* **2010**, *51*, 56–62. [[CrossRef](#)]
50. Mochizuki, M.; Katsuyama, J.; Higuchi, R.; Toyoda, M. Study of Residual Stress Distribution at Start-Finish Point of Circumferential Welding Studied by 3D-Fem Analysis. *Weld. World* **2005**, *49*, 40–49. [[CrossRef](#)]
51. Hempel, N.; Nitschke-Pagel, T.; Dilger, K. Residual stresses in multi-pass butt-welded ferritic-pearlitic steel pipes. *Weld. World* **2015**, *59*, 555–563. [[CrossRef](#)]
52. Benyounis, K.Y.; Olabi, A.G.; Hashmi, M. Residual Stresses Prediction for CO₂ Laser Butt-Welding of 304-Stainless Steel. *Appl. Mech. Mater.* **2006**, *3–4*, 125–130. [[CrossRef](#)]
53. Rong, Y.; Xu, J.; Huang, Y.; Zhang, G. Review on finite element analysis of welding deformation and residual stress. *Sci. Technol. Weld. Join.* **2018**, *23*, 198–208. [[CrossRef](#)]
54. Kong, F.; Ma, J.; Kovacevic, R. Numerical and experimental study of thermally induced residual stress in the hybrid laser–GMA welding process. *J. Mater. Process. Technol.* **2011**, *211*, 1102–1111. [[CrossRef](#)]
55. Buschenhenke, F.; Hofmann, M.; Seefeld, T.; Vollertsen, F. Distortion and residual stresses in laser beam weld shaft-hub joints. *Phys. Procedia* **2010**, *5*, 89–98. [[CrossRef](#)]
56. Nilsson, P.; Hedegård, J.; Al-Emrani, M.; Atashipour, S.R. The impact of production-dependent geometric properties on fatigue-relevant stresses in laser-welded corrugated core steel sandwich panels. *Weld. World* **2019**, *63*, 1801–1818. [[CrossRef](#)]
57. Wang, J.; Ren, L.; Xie, L.; Xie, H.; Ai, T. Maximum mean principal stress criterion for three-dimensional brittle fracture. *Int. J. Solids Struct.* **2016**, *102–103*, 142–154. [[CrossRef](#)]
58. Ben Salem, G.; Chapuliot, S.; Blouin, A.; Bompard, P.; Jacquemoud, C. Brittle fracture analysis of Dissimilar Metal Welds between low-alloy steel and stainless steel at low temperatures. *ProcediaStruct. Integr.* **2018**, *13*, 619–624. [[CrossRef](#)]
59. Casalino, G.; Angelastro, A.; Perulli, P.; Casavola, C.; Moramarco, V. Study on the fiber laser/TIG weldability of AISI 304 and AISI 410 dissimilar weld. *J. Manuf. Process.* **2018**, *35*, 216–225. [[CrossRef](#)]
60. Eisazadeh, H.; Achuthan, A.; Goldak, J.; Aidun, D. Effect of material properties and mechanical tensioning load on residual stress formation in GTA 304-A36 dissimilar weld. *J. Mater. Process. Technol.* **2015**, *222*, 344–355. [[CrossRef](#)]
61. Anawa, E.; Olabi, A.-G. Control of welding residual stress for dissimilar laser welded materials. *J. Mater. Process. Technol.* **2008**, *204*, 22–33. [[CrossRef](#)]
62. Yao, C.; Xu, B.; Zhang, X.; Huang, J.; Fu, J.; Wu, Y. Interface microstructure and mechanical properties of laser welding copper–steel dissimilar joint. *Opt. Lasers Eng.* **2009**, *47*, 807–814. [[CrossRef](#)]
63. Prabakaran, M.; Kannan, G.R. Optimization and metallurgical studies of CO₂ laser welding on austenitic stainless steel to carbon steel joint. *Ferroelectrics* **2017**, *519*, 223–235. [[CrossRef](#)]
64. Perricone, M.J.; Dupont, J.N.; Anderson, T.D.; Robino, C.V.; Michael, J.R. An Investigation of the Massive Transformation from Ferrite to Austenite in Laser-Welded Mo-Bearing Stainless Steels. *Met. Mater. Trans. A* **2010**, *42*, 700–716. [[CrossRef](#)]
65. Nikulina, A.A.; Bataev, I.; Smirnov, A.I.; Popelyukh, A.I.; Burov, V.; Veselov, S.V. Microstructure and fracture behaviour of flash butt welds between dissimilar steels. *Sci. Technol. Weld. Join.* **2014**, *20*, 138–144. [[CrossRef](#)]
66. Taban, E.; Deleu, E.; Dhooge, A.; Kaluc, E. Laser welding of modified 12% Cr stainless steel: Strength, fatigue, toughness, microstructure and corrosion properties. *Mater. Des.* **2009**, *30*, 1193–1200. [[CrossRef](#)]
67. Rossini, M.; Spena, P.R.; Cortese, L.; Matteis, P.; Firrao, D. Investigation on dissimilar laser welding of advanced high strength steel sheets for the automotive industry. *Mater. Sci. Eng. A* **2015**, *628*, 288–296. [[CrossRef](#)]
68. Ceglarek, D.; Colledani, M.; Váncza, J.; Kim, D.Y.; Marine, C.; Kogel-Hollacher, M.; Mistry, A.; Bolognese, L. Rapid deployment of remote laser welding processes in automotive assembly systems. *CIRP Ann.* **2015**, *64*, 389–394. [[CrossRef](#)]

69. Bakir, N.; Üstündağ, Ö.; Gumenyuk, A.; Rethmeier, M. Experimental and numerical study on the influence of the laser hybrid parameters in partial penetration welding on the solidification cracking in the weld root. *Weld. World* **2020**, *64*, 501–511. [[CrossRef](#)]
70. Kik, T.; Górká, J. Numerical Simulations of Laser and Hybrid S700MC T-Joint Welding. *Materials* **2019**, *12*, 516. [[CrossRef](#)] [[PubMed](#)]
71. Nagaraju, U.; Gowd, G.H.; Ahmad, R.M.I. Parametric analysis and evaluation of tensile strength for laser welding of dissimilar metal. *Mater. Today Proc.* **2018**, *5*, 7898–7907. [[CrossRef](#)]
72. Prabakaran, M.P.; Kannan, G.; Lingadurai, K. Microstructure and mechanical properties of laser-welded dissimilar joint of AISI316 stainless steel and AISI1018 low alloy steel. *Caribb. J. Sci.* **2019**, *53*, 978–998.
73. Ki, H.; Mazumder, J.; Mohanty, P.S. Modeling of laser keyhole welding: Part II. Simulation of keyhole evolution, velocity, temperature profile, and experimental verification. *Met. Mater. Trans. A* **2002**, *33*, 1831–1842. [[CrossRef](#)]
74. Esfahani, M.R.N.; Coupland, J.; Marimuthu, S. Microstructure and mechanical properties of a laser welded low carbon–stainless steel joint. *J. Mater. Process. Technol.* **2014**, *214*, 2941–2948. [[CrossRef](#)]
75. Pekkarinen, J.; Kujanpää, V. The effects of laser welding parameters on the microstructure of ferritic and duplex stainless steels welds. *Phys. Procedia* **2010**, *5*, 517–523. [[CrossRef](#)]
76. Vitek, J.M.; Dasgupta, A.; David, S.A. Microstructural modification of austenitic stainless steels by rapid solidification. *Met. Mater. Trans. A* **1983**, *14*, 1833–1841. [[CrossRef](#)]
77. Sinha, A.K.; Kim, D.Y.; Ceglarek, D. Correlation analysis of the variation of weld seam and tensile strength in laser welding of galvanized steel. *Opt. Lasers Eng.* **2013**, *51*, 1143–1152. [[CrossRef](#)]

Publisher’s Note: MDPI stays neutral with regard to jurisdictional claims in published maps and institutional affiliations.



© 2020 by the authors. Licensee MDPI, Basel, Switzerland. This article is an open access article distributed under the terms and conditions of the Creative Commons Attribution (CC BY) license (<http://creativecommons.org/licenses/by/4.0/>).